Water Air Soil Pollut (2023) 234:550
https://doi.org/10.1007/s11270-023-06547-7

# Apatite Ore-based Nanostructures: Novel and Eco-friendly Sorbent for Efficient Removal of Wastewater Containing $Pb^{2+}$ and $Fe^{3+}$

**Nguyen Thu Phuong · Nguyen Hong Nam · Cao Thi Hong · Dang Vu Qui Dac · Le Phuong Thu · Do Thi Hai · Magdalena Osial · Michael Giersig · Dinh Thi Mai Thanh**

Received: 11 October 2022 / Accepted: 22 July 2023


**Abstract** Global challenges in removing heavy metal ions from aquatic reservoirs require novel solutions, especially the application of environmentally friendly materials. This paper presented the efficient removal of $Fe^{3+}$ and $Pb^{2+}$ ions from wastewater by apatite ore-based nanostructures. The synthesized material exhibited a nanostructure with high thermal stability, high porosity, and negative surface potential, suitable for heavy metal removal in wastewater. The adsorption measurements performed in varying conditions (pH, mass of the adsorbent, and contact time onto the adsorbent) proved that even a few milligrams of the synthesized material could effectively absorb the lead and iron ions from the solution, reaching an effectiveness of about 90%. The maximum adsorption capacity was about 342.2 $mg{\cdot}g^{-1}$ for $Pb^{2+}$ and 1089.59 $mg{\cdot}g^{-1}$ for $Fe^{3+}$, while the adsorption isotherm determined with non-linear models undergoes the pseudo-first-order kinetics and Redlich-Peterson adsorption model. In addition, the thermodynamic parameters reveal the spontaneous process. Experiments conducted with industrial and craft-village wastewaters confirmed the high potential of the nanostructural hydroxyapatite as an efficient and affordable material for the removal of various pollutants from aqueous solutions in practical conditions.

**Keywords** Nanostructural hydroxyapatite · Apatite ore · Wastewater treatment · Heavy metal ions removal · Novel eco-friendly adsorbent · Adsorption

**Highlights**
- Hydroxyapatite exhibited a nanostructure with high thermal stability, high porosity, and negative surface potential.
- Maximum adsorption capacity is estimated at 342.2 $mg{\cdot}g^{-1}$ for $Pb^{2+}$ and 1089.59 $mg{\cdot}g^{-1}$ for $Fe^{3+}$
- Efficient removal of heavy metal ions with industrial and craft-village wastewaters.

N. T. Phuong · C. T. Hong · D. T. M. Thanh
Institute for Tropical Technology, Vietnam Academy of Science and Technology, 18 Hoang Quoc Viet, Cau Giay, Hanoi, Vietnam

N. H. Nam · D. V. Q. Dac · L. P. Thu · D. T. M. Thanh
University of Science and Technology of Hanoi, Vietnam Academy of Science and Technology, 18 Hoang Quoc Viet, Cau Giay, Hanoi, Vietnam

C. T. Hong · D. T. M. Thanh (✉)
Graduate University of Science and Technology, Vietnam Academy of Science and Technology, 18 Hoang Quoc Viet, Cau Giay, Hanoi, Vietnam
e-mail: dinh-thi-mai.thanh@usth.edu.vn; dtmthanh@itt.vast.vn

D. T. Hai
Hanoi University of Mining and Geology, 18 Pho Vien, Duc Thang, Bac Tu Liem, Hanoi, Vietnam

M. Osial · M. Giersig
Department of Theory of Continuous Media and Nanostructures, Institute of the Fundamental Technological Research, Polish Academy of Sciences, Pawińskiego 5B Str., 02-106 Warsaw, Poland

Published online: 14 August 2023

## 1 Introduction

Due to growing industrialization, water reservoirs are increasingly and widely polluted. Besides chemical compounds, the most problematic hazards to remove are heavy metal ions. Their appearance in the environment is mainly caused by anthropogenic activities, such as the disposal of batteries or electronic devices (Zhou et al., 2020). This issue is becoming more severe with the use of portable electronics. Heavy metals can be found even in tap water, leading to adverse health effects, including endocrine disruption and cancer (Andrade et al., 2020; Husband & Boxall, 2011). Among heavy metals, $Pb^{2+}$ and $Fe^{3+}$ are the two most common contaminants found in wastewater in Vietnam (Ibrahim & Abdel-Hameed, 2022; Huong et al., 2010). While lead is often present in wastewater of heavy industries, e.g., plating, tanning, and recycling industry, iron can be found in most old water pipes, including domestic water. Removal of these contaminants from aquatic reservoirs requires immediate and novel solutions.

Besides many methods, nanotechnology and nanomaterials seem to be low-cost, high-efficient, and scalable approaches (Duyen et al., 2018; Phuong et al., 2020; Tahoon et al., 2020). In recent years, heavy metal ions removal from wastewater has been achieved using different types of nanomaterials such as graphene flakes (Kong et al., 2021), activated carbon (Nga et al., 2021), carbon nanotubes (Vesali-Naseh et al., 2021), clays (Huang et al., 2020; Yadav et al., 2019), zeolites (Joseph et al., 2020), bio-adsorbents (Chen et al., 2021), silica (Li et al., 2021), hydroxyapatite (HAp), and apatites (Duyen et al., 2018; Nam et al., 2021; Phuong et al., 2020), where the apatite-based nanostructures are non-toxic and environmentally friendly sorbents. This material is well known for the water remediation from pollutants, including pharmaceutical-based compounds (Cleibson et al., 2021; Harja & Ciobanu, 2018), organic aromatic pollutants (Bouiahya et al., 2019; Li et al., 2021), and heavy metal ions (Duyen et al., 2018; Nam et al., 2021; Phuong et al., 2020). Moreover, this material exhibits very high stability in extreme thermal conditions and therefore can be applied in various industrial fields (Ramachandra et al., 1997). Hydroxyapatites can be synthesized chemically (Fahami et al., 2017), or from natural sources like animal bones (Bambaeero & Bazargan – Lari, 2021; Vahdat et al., 2019), or apatite ores (Phuong et al., 2020), where the synthesis from mineral ores is the most cost-effective technique. Using ores can significantly reduce production costs, bringing a promising solution for producing HAp at industrial scales. Up to the present, this approach is still relatively new with only a few studies found previously (Abdallah et al., 2021).

Given this, our study focuses on the preparation and application of nanostructural hydroxyapatite, one of the most effective materials that can be used for wastewater treatment using cost-effective and widely abundant apatite ores as a natural source of calcium and phosphates ions. The proposed material has a high removal capacity for $Pb^{2+}$ and $Fe^{3+}$ heavy metal ions, making it suitable to form less soluble mineral phases that are more stable in the environment than the $Pb^{2+}$ and $Fe^{3+}$ ions. Prior to the treatment of real wastewater, the adsorption studies were performed in the function of contact time, initial $Pb^{2+}$ and $Fe^{3+}$ concentration, pH, adsorbent mass, and temperature, as well as the kinetics and adsorption mechanism was studied.

## 2 Experimental

### 2.1 Nanostructural Hydroxyapatite Preparation

The apatite ore was collected from Lao Cai province, Vietnam. The nitric acid $HNO_3$ 63%, aqueous ammonia solution $NH_{3(aq)}$ 25%, and iron (III) chloride hexahydrate $FeCl_3{\cdot}6H_2O$ 99% having analytical grade were purchased from Xilong Scientific Co, China. The $Pb(NO_3)_2$ 99.5% with the analytical grade was supplied from Merck, Germany.

The raw apatite ore was initially milled into the powder and dried at 105°C in an oven. Then, the dry mass of about 1 g of apatite ore was treated with 20 mL of 1 M $HNO_3$ solution and stirred within the magnetic stirring bar at 400 rpm for 30 min at room temperature. Then, the precipitate was separated by filtration, and the obtained solution was used as a source of $Ca^{2+}$ and $PO_4^{3-}$ ions to prepare hydroxyapatite (HAp) with the use of the precipitating agent. The ammonia $NH_{3(aq)}$ solution was added dropwise until pH 10, maintaining the hydroxyapatite formation instead of the calcium phosphate compounds. Then, the white precipitate was filtered and washed with

distilled water until neutral pH. Next, the powder was dried at 105 °C overnight and had a phase structure of the hydroxyapatite (HAp) with a $pH_{pzc}$ of about 7.49 (Phuong et al., 2020).

### 2.2 Lead ($Pb^{2+}$) and Iron (III) ($Fe^{3+}$) Ions Adsorption Experiments

The adsorption experiments were performed using solutions containing $Pb^{2+}$ and $Fe^{3+}$ ions as follows: 50 mL of $Pb(NO_3)_2$ or $FeCl_3$ solutions at concentrations ranging from 5 to 400 mg·$L^{-1}$ was prepared. The adsorption studies were performed using different adsorbent amounts, from 0.001 to 0.17 g (dry basis). Experiments were also conducted in the function of pH ranging from pH 1 to pH 6 adjusted with HCl and NaOH and in the function of time (5 min, 10 min, 20 min, 30 min, 40 min, 60 min, 80 min, 100 min, and 120 min). $Pb^{2+}$ and $Fe^{3+}$ adsorption efficiency $H$ (%) and capacity ($Q$ (mg·$g^{-1}$)) were determined based on Eqs. (1) and (2):

$$H = \left(C_o - C_e\right).\frac{100}{C_o} \tag{1}$$

$$Q = \left(C_o - C_e\right).\frac{V}{m} \tag{2}$$

where $C_o$ (mg·$L^{-1}$) is the initial concentration of $Pb^{2+}$ and $Fe^{3+}$ ions in the solution, $C_e$ (mg·$L^{-1}$) is the heavy metal ions concentration at equilibrium, $V$ (L) is the solution volume ($V$ = 50 mL), and $m$ (g) is the amount of nanostructural hydroxyapatite.

### 2.3 Structural and Adsorption Analysis

The TGA-DTG analysis from room temperature to 800 °C at 5°C·$min^{-1}$ in the air was performed on a Macro-thermogravimetric system (CIRAD – France) to determine the thermal behaviors of HAp.

The surface morphology was studied using scanning electron microscopy (SEM), JSM-6510LV, JEOL Ltd. (Japan), and transmission electron microscopy (TEM) JEM-2100 JEOL Ltd. (Japan).

Before and after adsorption, the element composition of the material was determined by EDX analysis with X-Act (Oxford).

The surface functional groups were detected using an FTIR spectrometer (Nicolet iS10, Thermo Scientific) in a range of 400–4000 $cm^{-1}$.

The porous structures of hydroxyapatite were investigated using a Micromeritics 3Flex Adsorption Analyzer. The Brunauer–Emmett–Teller (BET) method was applied to estimate the total surface area and total pore volume of the material, while the micropore's and mesopore's surface area and volume were identified via the t-plot and BJH method, respectively. The surface potential onto HAp was determined using the dynamic light scattering method (DLS, SZ-100V2, Nanoparticle analyzer, Nanopartica, Horiba Scientific (Japan) in the charge range of about −200 to 200 mV at 25 °C).

The $Pb^{2+}$, $Fe^{3+}$, and $Ca^{2+}$ concentrations were determined by the Atomic Absorption Spectrometry (AAS) method at a wavelength of $\lambda$ = 217 nm, $\lambda$ = 248.3 nm, and $\lambda$ = 422.7 nm, respectively, on the AAS iCE 3500 Thermo Scientific (Germany).

The crystallinity of the hydroxyapatite before and after the adsorption was characterized by the phase component by X-ray diffraction (XRD), D8 ADVANCE-Bruker, $CuK_\alpha$ radiation ($\lambda$ = 1.54056 Å) with a step angle of 0.03°, the scanning rate of 0.04285° per second, and 2θ degree was measured in the range of 10–70°).

## 3 Results and Discussion

### 3.1 Characterization of Hydroxyapatite

#### *3.1.1 Morphology, Element Composition, and Surface Potential of Hydroxyapatite*

The morphology of HAp was determined using scanning electron microscopy (SEM, Fig. 1) and transmission electron microscopy (TEM, Fig. 2). Figure 1 shows nanostructured grains distributed uniformly within the whole volume. The mapping image of different elements on the surface of the hydroxyapatite is measured by the EDX technique. It can be seen that the main surface elements, which are Ca, P, and O, are uniformly distributed on the whole surface of the sample.

Based on the TEM analysis (Fig. 2), it can be observed that HAp grains have a size of about 20 nm. The overlapping of the particles is caused by the drying of the sample from the aqueous solution

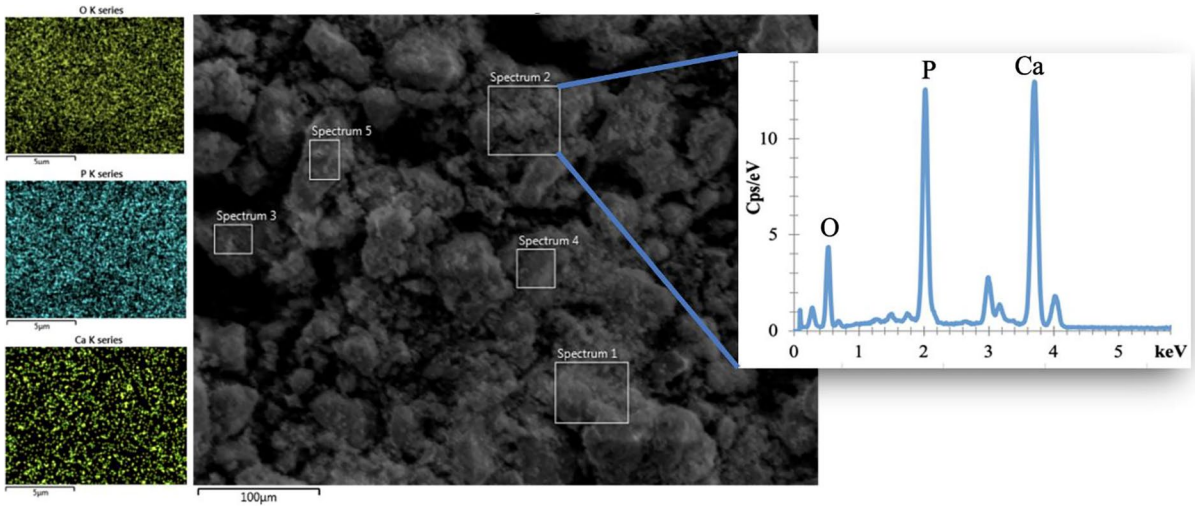


**Fig. 1** SEM-EDX image of HAp

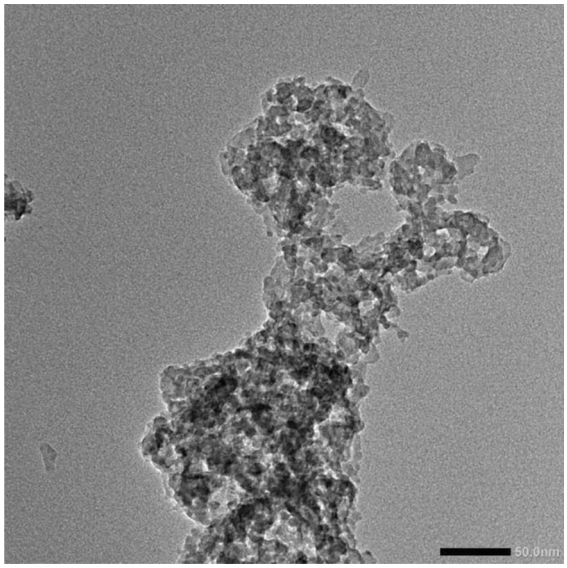


**Fig. 2** TEM image of the hydroxyapatite. The scale bar in the TEM image is about 50 nm

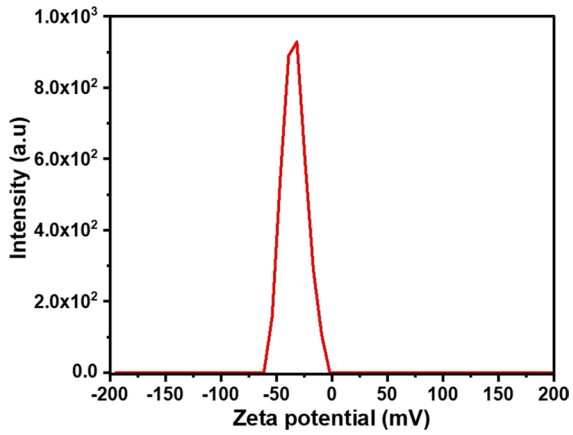


**Fig. 3** Zeta potential of the hydroxyapatite

pushing particles to move close to each other. Despite the aggregation, each individual particle possesses a nanostructural structure.

The surface charge of the nanostructural hydroxyapatite was determined by the zeta potential measurements (Fig. 3). The obtained value of the surface potential is about −34.4 mV for the presence of the hydroxyl groups. A negative value of the surface potential suggests a strong interaction of the material with the heavy metals cations, hence improving the effectiveness in the removal of these ions from aquatic systems (Ragab et al., 2019).

### *3.1.2 $N_2$ Adsorption-Desorption Isotherms*

The porosity of the hydroxyapatite was analyzed from the $N_2$ adsorption-desorption isotherms (Fig. 4). The material exhibited type IV(a) isotherms in the IUPAC classification with a large-range hysteresis loop.

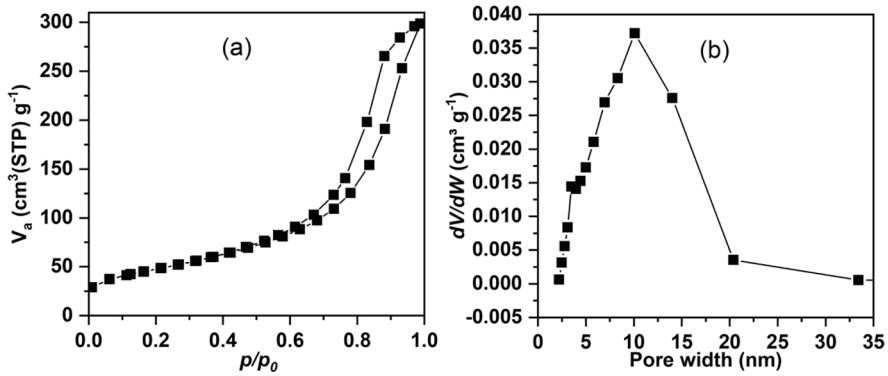


**Fig. 4** $N_2$ adsorption-desorption isotherms of HAp

**Table 1** Specific surface area and pore volume of hydroxyapatite

| $S_{Total}$ ($m^2 \cdot g^{-1}$) | $V_{Total}$ ($cm^3 \cdot g^{-1}$) | $V_{Micro}$ ($cm^3 \cdot g^{-1}$) | $V_{Meso}$ ($cm^3 \cdot g^{-1}$) | $d_{Mean\ pore}$ (nm) |
|---|---|---|---|---|
| 169.92 | 0.45 | 0 | 0.45 | 9.6 |

This phenomenon can be associated with capillary condensation (Satoshi et al., 2008), whereby a gas is condensed to a liquid-like phase in a pore at a pressure $p < p_o$. This result suggests that mesopores greater than ~4 nm are dominant in the material. Moreover, the hysteresis loop can be classified as Type H3, where complex pore structures exist and networking effects are important. The presence of ink-bottle pores may exist, suggesting a good capturing potential of pollutants for this material when used as an adsorbent. The total surface area ($S_{Total}$) estimated by the BET method as well as the total pore volume ($V_{Total}$), the micropore volume ($V_{Micro}$), and mesopore volume ($V_{Meso}$) estimated by the t-plot and BJH methods are presented in Table 1.

The $S_{Total}$ and $V_{Total}$ of the hydroxyapatite are comparable to that of other highly porous HAp (Cedric et al., 2007), opening a great potential for the use of this material as a commercial product. The pore size distribution confirmed that the material was mostly composed of mesopores with pore widths in the range of 2.5 to 20 nm (Fig. 4b).

### *3.1.3 Thermal Behavior of Hydroxyapatite*

The TGA-DTG curves of HAp from room temperature to 800 °C in air, at a heating rate of 5 °C min$^{-1}$, are presented in Fig. 5. It can be seen in Fig. 5 that

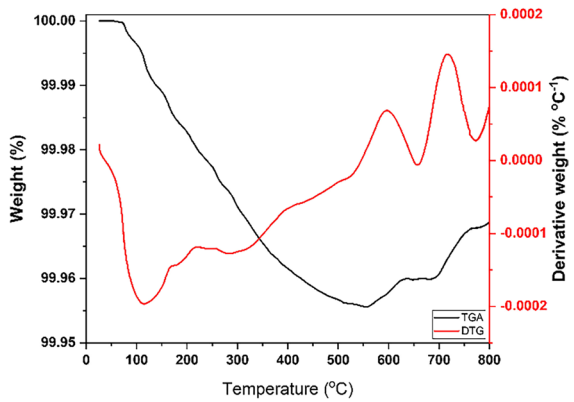


**Fig. 5** TGA-DTG curves of HAp

the total weight loss of HAp is about only 0.05%, which is insignificant compared to some other HAp synthesized in previous studies (Marjan et al., 2020; Pramod et al., 2016; Slavica et al., 2001). The first peak at around 100 °C in the DTG corresponded to the remaining moisture released from the material. The main weight loss occurred between 100 and 550 °C with a very small rate of around 0.0001%·°C$^{-1}$. This result indicates that HAp is very stable and can maintain its chemical integrity, even under severe thermal conditions.

## 3.2 Effect of Adsorbent Mass and Contact Time

The effect of the adsorbent mass on the removal of $Pb^{2+}$ and $Fe^{3+}$ from aqueous solutions was investigated in this study. Therefore, 1–170 mg of adsorbent was added into different beakers for 60 min with the pH of $Pb^{2+}$ solution of 4 and 2.65 in the case of $Fe^{3+}$. As shown in Fig. 6a, the adsorption efficiency

increases rapidly from 39 to 100%, corresponding to an increase in adsorbent mass ($m$) from 3 to 10 mg for $C_0$ = 50 mg·L$^{-1}$ and contact time $t$ = 60 min. Meanwhile, $Fe^{3+}$ ion removal efficiency increased dramatically from 35 to 93%, respectively (Fig. 6b). The results also showed that the adsorption capacity of $Fe^{3+}$ ions by HAp is higher than that of $Pb^{2+}$ when the adsorbent mass increases. However, the amount of adsorbent continued to increase by more than 10 mg, and the ion removal efficiency increased insignificantly (in the case of $Fe^{3+}$) or slightly decreased ($Pb^{2+}$ case). It is concluded that the optimal amount of the nanostructural HAp is clearly shown to be around 10 mg, demonstrating its excellent efficacy in ion removal even with only a tiny amount of the adsorbent. It can be seen that the heavy metal ion (HMI) absorption was enhanced due to an increase in the adsorbent dosage and surface area available. After full adsorption of HMI in solution, the amount of HMI adsorbed per unit mass of HAp decreased due to excess accessible sorption sites. The splitting effect of the concentration gradient may possibly be contributing to the decline.

The effect of different contact times $t$, from 5 to 120 min, on the heavy metal ions' adsorption was presented in Fig. 7. It can be seen that the adsorption trend is quite similar for both ions. For an increase of $t$ from 5 to 40 min, the $Pb^{2+}$ adsorption efficiency rises from 27 to 97%, and the capacity rises from 71.87 to 269.52 mg·g$^{-1}$. However, after 40 min, these parameters remain stable and an adsorption equilibrium is reached. For the removal of $Fe^{3+}$ using hydroxyapatite, 80 min was selected as the optimal time, with an adsorption efficiency and capacity of 93% and 201.82 mg·g$^{-1}$, respectively. The fast first-stage adsorption may be due to the presence of a large number of vacant adsorption sites. When heavy metal ions are adsorbed on HAp materials' adsorption sites, the number of these sites diminishes and the slope becomes flat as the adsorption rate lowers (Sugashini & Begum, 2013).

### 3.3 Effect of pH

The adsorption efficiency was also measured in the function of pH, ranging from 2.5 to 6 for $Pb^{2+}$ and 1 to 4 for $Fe^{3+}$, assuming the pH point zero charge ($pH_{pzc}$) of 7.49 (Phuong et al., 2020). The surface charge was modified depending on the pH, with $pH_{solution} < pH_{pzc}$, the surface of the adsorbent having a positive charge, and vice versa. The adsorption efficacy as a function of pH may be described using the $pH_{pzc}$ value.

In the case of the $Pb^{2+}$ solution, precipitation was seen at pH values greater than 6, but for $Fe^{3+}$, the critical pH value for precipitation was greater than 4, similar to the effect demonstrated by Mavropoulos et al. (2002) and Hashimoto et al. (2009). The surface of HAp has a positive charge when the pH is lower than $pH_{pzc}$; hence, electrostatic force occurs. As a result, these measurements were carried out in

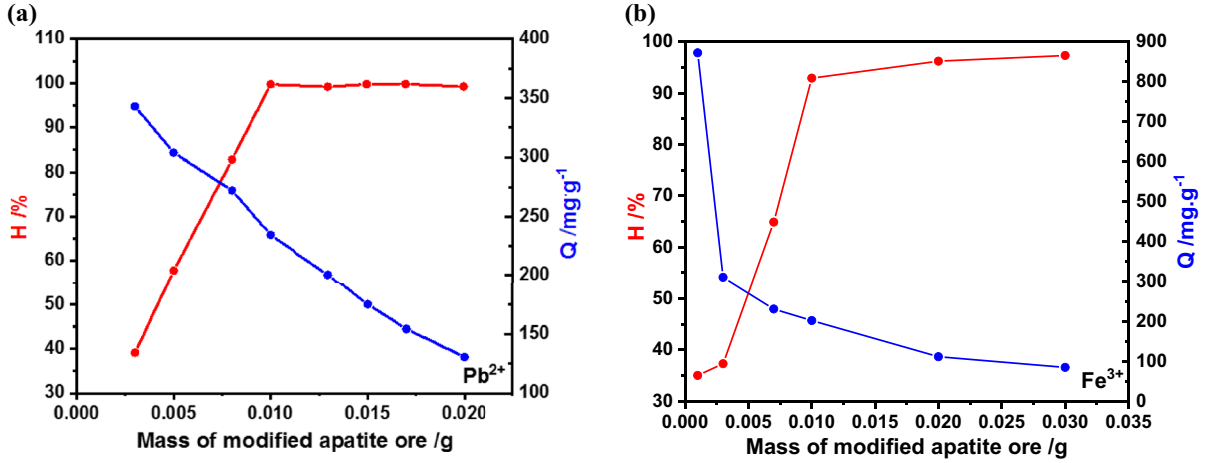


**Fig. 6** Effect of sorbent dose on adsorption efficiency and capacity for (**a**) $Pb^{2+}$ and (**b**) $Fe^{3+}$ ($C_0$ = 50 mg·L$^{-1}$, $t$ = 60 min)

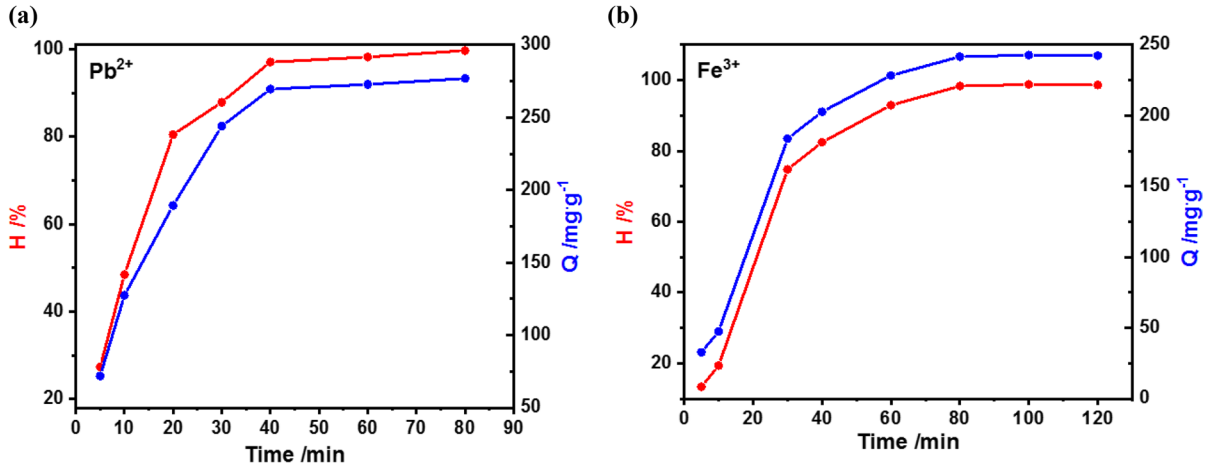


**Fig. 7** Effect of contact time on adsorption efficiency and capacity for (**a**) $Pb^{2+}$ and (**b**) $Fe^{3+}$ ($C_0$ = 50 mg·$L^{-1}$, $pH_0$, $m$ = 10 mg)

relation to pH, with $m$ = 10 mg and $C_0$ = 50 mg.$L^{-1}$, $t$ = 80 min.

The rivalry between $H^+$ ions and heavy metal ions causes less efficient adsorption, as seen in Fig. 8. All the data reveal that the optimum adsorption efficiency and capacity at the initial pH for $Pb^{2+}$ is 4 and the initial pH for $Fe^{3+}$ is 2.65.

### 3.4 Effect of Initial $Pb^{2+}$ and $Fe^{3+}$ Concentration

To determine the influence of the initial concentration on the adsorption efficiency and capacity of the hydroxyapatite, the concentration $C$ of $Pb^{2+}$ solution was varied from 20 to 150 mg·$L^{-1}$, and for the $Fe^{3+}$ solution, the concentration was changed from 5 to 400 mg·$L^{-1}$ at $t$ = 80 min. Figure 9 reveals a decrease in the efficiency and an increase of the capacity with the rise of the initial ions concentration, indicating that for particular values, adsorption reaches saturation. There is a specified number of adsorption pores for a given amount of hydroxyapatite. In the case of all the adsorption pores being filled by $Pb^{2+}$ and $Fe^{3+}$ ions, the adsorption capacity has nearly no change when the concentration of heavy metals increases.

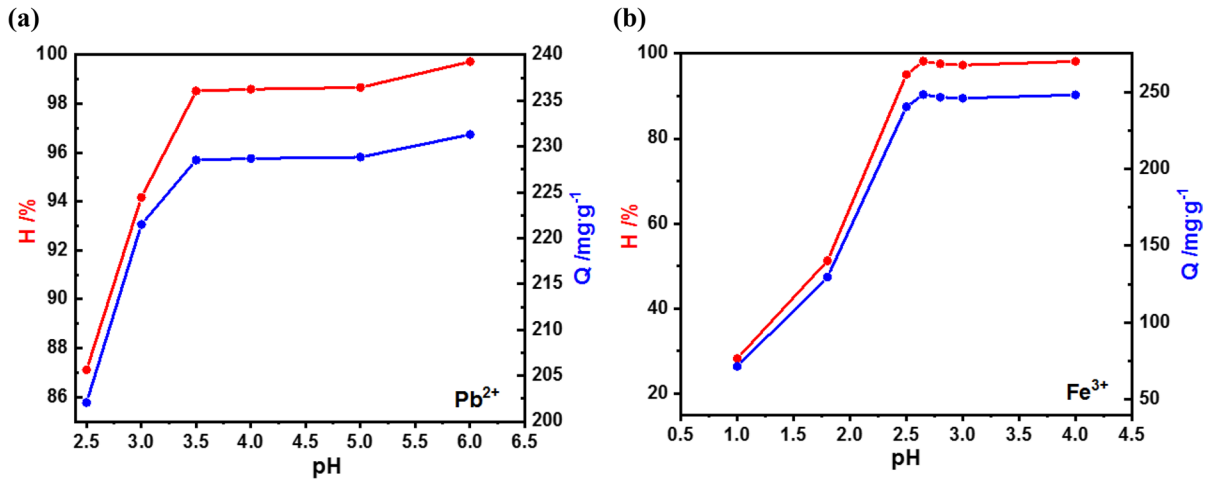


**Fig. 8** Effect of pH on adsorption efficiency and capacity for (**a**) $Pb^{2+}$ and (**b**) $Fe^{3+}$

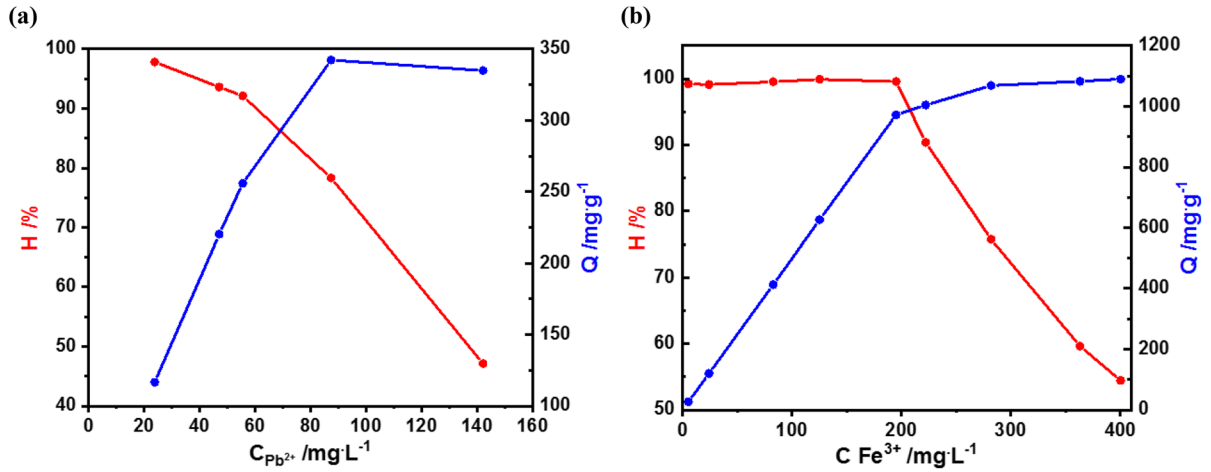


**Fig. 9** Effect of $Pb^{2+}$ (**a**) and $Fe^{3+}$ (**b**) initial concentration on adsorption efficiency and capacity ($m$ = 10 mg, $pH_0$)

### 3.5 Adsorption Kinetics

A comprehensive study of adsorption processes will be incomplete if the structure and dynamics of its many aspects, as well as how they interact, are not effectively represented. As a result, considerable research into adsorption thermodynamics in combination with adsorption kinetics is required.

The adsorption mechanism was determined based on the experimental results. To investigate the kinetics of that process, Lagergren's pseudo-first-order law and McKay-Ho's pseudo-second-order law models were used, where both equations of the two models are given in Eqs. (3) and (4), respectively (Tran et al., 2017):

$$Q_t = Q_e\left(1 - e^{-k_1 t}\right) \tag{3}$$

where $Q_t$ (mg·g$^{-1}$) is the adsorption capacity at time $t$, $Q_e$ (mg·g$^{-1}$) is the adsorption capacity at equilibrium, and $k_1$ (min$^{-1}$) is the pseudo-first-order adsorption rate constant.

$$Q_t = \frac{{Q_e}^2 k_2 t}{Q_e k_2 t + 1} \tag{4}$$

where $k_2$ (g·min$^{-1}$·mg$^{-1}$) is the pseudo-second-order rate constant for adsorption.

Non-linear models were used to determine the amount adsorbed in the equilibrium, rate constant, and correlation coefficient. Figure 10 shows both non-linear models for $Pb^{2+}$ and $Fe^{3+}$ ions. Based on the higher values of $R^2$ in the adsorption of metal ions, the pseudo-first-order of kinetics was proposed. The parameters estimated based on that model are presented in Table 2. The value $Q_e$ between from experimental and calculation is not remote. The non-linear form of kinetic models retains the distribution of the error and kinetic factor unchanged in both axes (Ganguli et al., 2020).

### 3.6 Adsorption Analysis

The equilibrium isotherm is described by the surface characteristics and affinity of the sorbent that is expressed in the values of the sorption isotherm's constants. The equilibrium is reached when the adsorbate concentration in the bulk solution equals the sorbent interface concentration. As follows, equilibrium data from the sorption process may be modeled using different commonly used equilibrium equations, so in our experiments, the $Pb^{2+}$ and $Fe^{3+}$ adsorption process on HAp was described by using the Langmuir, Freundlich, and Redlich-Peterson models. Tests on adsorption were carried out by mixing 10 mg of the hydroxyapatite with 50 mL of $Pb^{2+}$ or $Fe^{3+}$ having different concentrations in a 100-mL Duran flask and then stirring at 400 rpm for 80 min. The adsorption isotherms for $Pb^{2+}$ and $Fe^{3+}$ are presented in Fig. 11, where the simulations of the Langmuir, Freundlich, and Redlich-Peterson models were made based on Eqs. (5)–(7) as follows (Lima et al., 2015; Tran et al., 2017; Tran et al., 2021):

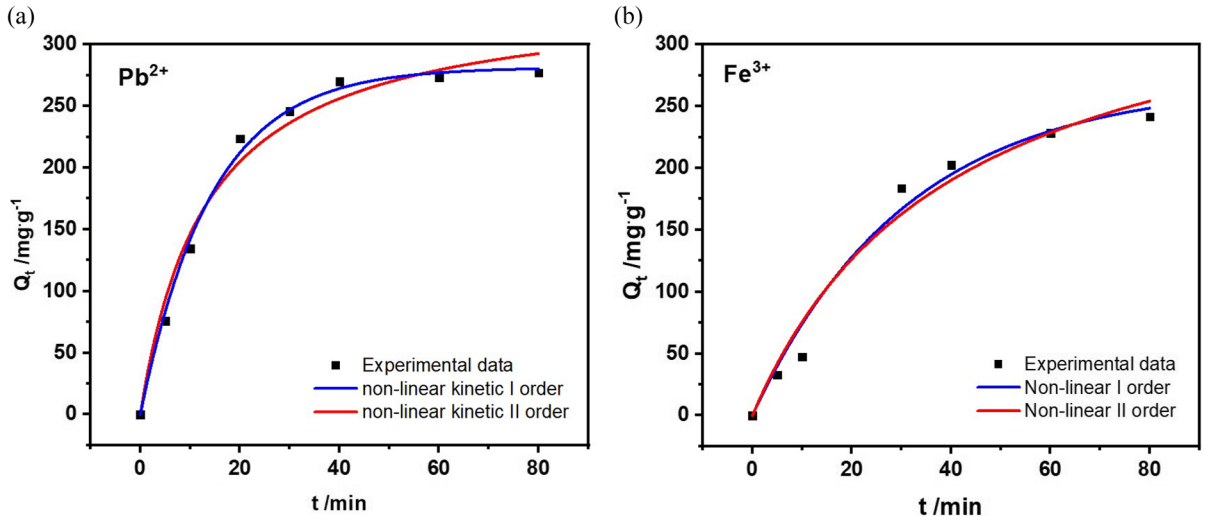


**Fig. 10** Adsorption data modeled using Lagergren's pseudo-first-order law and McKay and Ho's pseudo-second-order kinetic models for (**a**) $Pb^{2+}$ and (**b**) $Fe^{3+}$

**Table 2** Parameters of $Pb^{2+}$ and $Fe^{3+}$ removal process calculated using Lagergren's pseudo-first-order non-linear models

| | Qe.exp ($mg \cdot g^{-1}$) | Qe.cal ($mg \cdot g^{-1}$) | $k_2$ ($g \cdot mg^{-1} \cdot min^{-1}$) | $R^2$ |
|---|---|---|---|---|
| $Pb^{2+}$ | 276.870 | 281.238 | 0.07013 | 0.9955 |
| $Fe^{3+}$ | 242.476 | 268.795 | 0.03225 | 0.9780 |

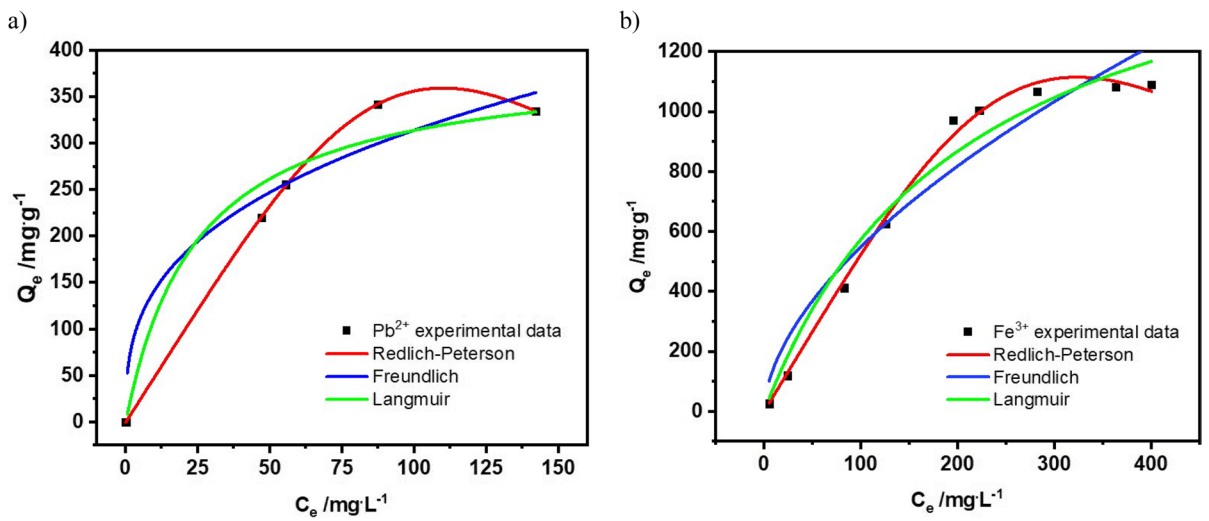


**Fig. 11** Non-linear adsorption isotherms for (**a**) $Pb^{2+}$ and (**b**) $Fe^{3+}$ onto hydroxyapatite

$$\text{Langmuir}: Q_e = \frac{Q_{\max} \times K_L \times C_e}{1 + K_L \times C_e}, \quad (5)$$

where $Q_e$ stands for the amount of adsorbent in equilibrium ($mg \cdot g^{-1}$), $Q_{\max}$ is the maximal amount adsorbed ($mg \cdot g^{-1}$), $K_L$ stands for the Langmuir

equilibrium constant ($L{\cdot}g^{-1}$), and $C_e$ stands for concentration of ions ($mg{\cdot}L^{-1}$).

$$\text{Freundlich}: Q_e = K_F \times {C_e}^{1/n}, \tag{6}$$

where $K_F$ is the Freundlich constant with multilayer adsorption relating to the bond strength ($mg{\cdot}g^{-1}(L{\cdot}g^{-1})^n$) and $n$ is the dimensionless parameter defining adsorption.

$$\text{Redlich}-\text{Peterson}: Q_e = \frac{K_{RP}C_e}{1 + a_{RP} \times {C_e}^g}, \tag{7}$$

where $K_{RP}$ is the Redlich-Peterson constant ($L{\cdot}g^{-1}$), $a_{RP}$ stands for the Redlich-Peterson equilibrium constant $(mg{\cdot}L^{-1})^{-g}$, and $g$ is a constant dimensionless parameter.

According to the Langmuir equation, a monolayer of adsorbate on the absorber's surface is required for maximal adsorption. For Freundlich's model, a broad variety of concentrations may be taken into account by taking into consideration surface heterogeneity, as well as the exponential distribution of active sites and their related energies. Following, the Redlich-Peterson model considers the limitations of the Langmuir and Freundlich models. It can be used to demonstrate adsorption equilibrium over a wide range of concentrations of adsorbate (Tran et al., 2017; Lima et al., 2021).

Figure 11 shows the graphical representation of these models, where the values of the correlation coefficient $R^2$ obtained from particular models were used to determine the best fitting. In the case of the $Pb^{2+}$ adsorption, see Fig. 11a, it can be seen that the $R^2$ for Redlich-Peterson isotherm is higher (0.9996) than for Langmuir isotherm (0.9459) and Freundlich (0.7523) isotherm. Similar to these results, for the $Fe^{3+}$, the value of the correlation coefficient was also higher for the Redlich-Peterson isotherm (0.9964) than for the Langmuir isotherm (0.9691) and Freundlich (0.9325) isotherm. Therefore, it can be seen that the adsorption undergoes the Redlich-Peterson model, which assumes that adsorbate is applicable either in the homogeneous or heterogeneous system. The parameters characteristic to all these models are presented in Table 3, showing that the $Q_{max}$ determined from the Langmuir isotherm is about 392.36 $mg{\cdot}g^{-1}$ for $Pb^{2+}$ and 1781.68 $mg{\cdot}g^{-1}$ for $Fe^{3+}$.

According to the $Pb^{2+}$ removal, the literature shows that an increase in metal ion concentration leads to an increase in the number of metal ions present at the adsorbent surface, which in turn leads to an increase in the likelihood of adsorption (Sridevi et al., 2015). This outcome is compatible with S.T. Ramesh's research (Ramesh et al., 2013). They demonstrated that the maximal adsorption capacity of synthetic HAp is 357.14 mg Pb(II)$\cdot L^{-1}$ with 0.12 g HAp$\cdot L^{-1}$ optimum dosage and that the $Pb^{2+}$ adsorption kinetics match the pseudo-second-order reaction and the Langmuir adsorption isotherm model. In the case of composites, Zhang et al. proposed the Langmuir model for $Pb^{2+}$ removal of hydroxyapatite/calcium silicate hydrate (HAp/C-H-S), where the adsorption capacity reaches 946.7 $mg{\cdot}g^{-1}$ for highly developed surface (Zhang et al., 2018). Comparing the results with the literature, it is seen that the effectiveness of heavy metal ions removal with bare HAp can differ for different ions. For example, Lusvardi et al. studied the $Cd^{2+}$ and $Pb^{2+}$ removal by synthetic HAp, also indicating a different behavior of $Pb^{2+}$ removal with respect to $Cd^{2+}$ (Lusvardi et al., 2002). Iconaru et al. showed an adsorption capacity of about 99.3 $mg{\cdot}g^{-1}$ with the nanostructural hydroxyapatite using the Langmuir model (Iconaru et al., 2018). Baileliez et al. referred to the adsorption capacity of about 320 $mg{\cdot}g^{-1}$ with the HAp particles sized ~16 μm, where the adsorption undergoes the Langmuir-Freundlich model (Bailliez et al., 2004). Minh et al.

**Table 3** The parameters of the selected adsorption isotherm models obtained from Fig. 11 with the plot of $Q_e$ ($mg{\cdot}g^{-1}$) *vs.* $C_e$ ($mg{\cdot}L^{-1}$)

| | $Pb^{2+}$ | $Fe^{3+}$ |
|---|---|---|
| $Q_{max\text{-}exp}$ ($mg{\cdot}g^{-1}$) | 342.20 | 1089.59 |
| Langmuir model | | |
| $Q_L$ ($mg{\cdot}g^{-1}$) | 392.36 | 1781.68 |
| $K_L$ ($L{\cdot}mg^{-1}$) | 0.0402 | 0.0047 |
| Adj $R^2$ | 0.9459 | 0.9691 |
| Freundlich model | | |
| $K_F$ ($mg{\cdot}g^{-1}$) | 64.3120 | 38.9583 |
| $n_F$ | 0.3445 | 0.5748 |
| Adj $R^2$ | 0.7523 | 0.9325 |
| Randles-Peterson | | |
| $K_{RP}$ ($L{\cdot}g^{-1}$) | 4.8714 | 5.34261 |
| $a_{RP}$ $(L{\cdot}mg^{-1})^g$ | 3.0417e-7 | 4.56672e-8 |
| $g$ | 3.0406 | 2.8211 |
| Adj $R^2$ | 0.9996 | 0.9964 |

showed that the effectiveness of HAp over the $Pb^{2+}$ removal depends on experimental conditions and can vary from 84 to even 620 $mg{\cdot}g^{-1}$ (Minh et al., 2013). Another study presented by Meski et al. shows the results for carbonized HAp prepared from the domestic hen waste egg shells, where the $Pb^{2+}$ undergoes an adsorption Langmuir mechanism with a maximum adsorption capacity of 500 $mg{\cdot}g^{-1}$ at 25 °C and 35 °C (Meski et al., 2010).

Furthermore, the $Fe^{3+}$ adsorption capacity measured in this study (1089.59 $mg{\cdot}g^{-1}$) was significantly higher than the maximum iron adsorption capacity in prior investigations (55.25 $mg.g^{-1}$), where the adsorption follows pseudo-second-order kinetics (Brundavanam et al., 2015). Some works refer to the formation of many defects in the HAp structure that influence the effectiveness in the removal of particular compounds (Avakyan et al., 2021; Jiang et al., 2002). However, as mentioned above, the effectiveness of water purification with HAp depends on the experimental conditions. In work presented by Billah et al., the adsorption capacity with the fluorapatite is about 19.88 $mg{\cdot}g^{-1}$, where the adsorption mechanism fits the Langmuir model and the kinetics follows the pseudo-second-order (Billah et al., 2021). Another work shows the 2.54 $mg{\cdot}g^{-1}$ adsorption capacity with cow bone-derived HAp (Olabiyi & Adekola, 2018). The kinetic and the isotherm models are proposed to be pseudo-second-order and Langmuir models, respectively.

The adsorption capacity for the $Pb^{2+}$ removal is similar to the data presented in the literature, while the values for $Fe^{3+}$ removal are much lower than the experimental data obtained in this work. The kinetic models differ from the literature in what can be caused by the application of linear models. This shows that cost-effective and widely available materials like apatite ore in Vietnam may be employed to manufacture extremely effective adsorbents.

### 3.7 Temperature Effect

The experiments were also performed in function of temperature, indicating that along with an increase in temperature, the adsorption efficiency and capacity also rise (Table 4). Then, the standard Gibbs free energy change ($\Delta G°$), the enthalpy change ($\Delta H°$), and the entropy change ($\Delta S°$) of the adsorption of $Pb^{2+}$ and $Fe^{3+}$ onto the hydroxyapatite were estimated within Eqs. (8) and (9):

$$\Delta G° = -RT\ln K_d \tag{8}$$

$$\ln K_d = -\frac{\Delta H^0}{R}\, x\, \frac{1}{T} + \frac{\Delta S^0}{R} - \frac{\Delta H^0}{R} x \frac{1}{T} + \frac{\Delta S^0}{R} \tag{9}$$

where $R$ is the universal gas constant (8.314 $Jmol^{-1}K^{-1}$), $T$ is the temperature (K), and $K_d$ is the equilibrium constant.

The intercept and slope of the plot of $\ln(K_d)$ versus $(1/T)$ (Fig. 12) give the values of $\Delta G°$, $\Delta H°$, and $\Delta S°$, which are summarized in Table 5. The positive values of $\Delta H°$ and the negative values of $\Delta G°$ confirm the spontaneous and endothermic character of the ions' adsorption. The values of $\Delta G°$ are smaller than the value of physical adsorption (−20 to 0 $kJ{\cdot}mol^{-1}$) and chemisorption range (−80 to −400 $kJ{\cdot}mol^{-1}$), suggesting that the adsorption of $Pb^{2+}$ and $Fe^{3+}$ onto that HAp has a physisorption character. The randomness at the adsorbate-adsorbant interface is confirmed with positive values of $\Delta S°$ (Thuy et al., 2021).

**Table 4** $H$ (%), $Q_e$ ($mg{\cdot}g^{-1}$), and $K_d$ as a function of temperature in $Pb^{2+}$ and $Fe^{3+}$ adsorption process ($t$ = 80 min, $m$ = 0.005 g, $pH_0$)

| Temperature (K) | $C_o$ ($mg{\cdot}L^{-1}$) | $C_e$ ($mg{\cdot}L^{-1}$) | $H$ (%) | $Q_e$ ($mg{\cdot}g^{-1}$) | $K_d = Q_e/C_e$ | $\ln K_d$ | $1/T$ |
|---|---|---|---|---|---|---|---|
| $Pb^{2+}$ | | | | | | | |
| 298 | 42.47 | 22.54 | 47 | 199.28 | 8.84 | 2.18 | 0.0034 |
| 338 | | 13.59 | 68 | 288.79 | 21.25 | 3.06 | 0.0030 |
| 348 | | 11.37 | 73 | 311.01 | 27.36 | 3.31 | 0.0029 |
| $Fe^{3+}$ | | | | | | | |
| 298 | 50.92 | 33.18 | 34.83 | 177.33 | 5.34 | 1.68 | 0.0034 |
| 328 | | 31.05 | 39.02 | 198.69 | 6.40 | 1.86 | 0.0030 |
| 348 | | 28.49 | 44.06 | 224.33 | 7.88 | 2.06 | 0.0029 |

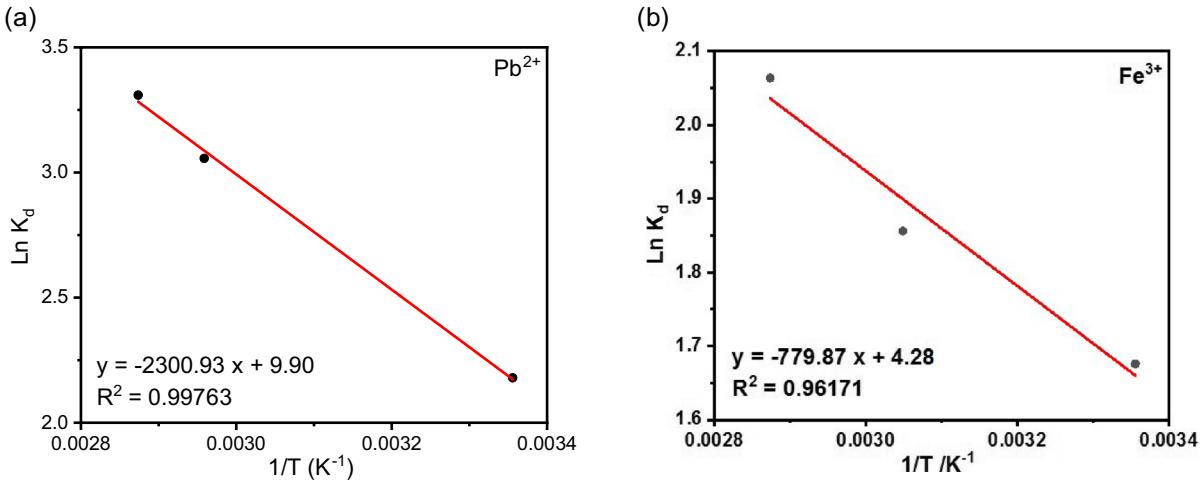


**Fig. 12** The relationship of $\mathrm{Ln}K_d$ and $1/T$ in the case of $Pb^{2+}$ (**a**) and $Fe^{3+}$ (**b**)

**Table 5** The thermodynamic parameters $\Delta H°$, $\Delta S°$, and $\Delta G°$ in the case of $Pb^{2+}$ and $Fe^{3+}$

| Temperature (K) | $\Delta H°$ (kJ·mol$^{-1}$) | $\Delta S°$ (kJ·mol$^{-1}$·K$^{-1}$) | $\Delta G° = \Delta H° - T.\Delta S°$ (kJ·mol$^{-1}$) |
|---|---|---|---|
| $Pb^{2+}$ | | | |
| 298 | 19.13 | 0.082 | −5.39 |
| 338 | | | −8.68 |
| 348 | | | −9.50 |
| $Fe^{3+}$ | | | |
| 298 | 6.48 | 0.036 | −4.11 |
| 328 | | | −5.18 |
| 348 | | | −5.89 |

## 3.8 Wastewater Treatment

In complement to our detailed investigations of the heavy metal ions removal in the laboratory, real wastewater was tested to confirm the effectiveness of our proposed adsorbent in practical conditions. The wastewater was collected at a plating company in Noi Bai Industrial Zone and Trieu Khuc craft village, Hanoi, Vietnam. The sample had white-bluish color and a metallic odor. Analysis results (Table 6) show that the $Fe^{3+}$ concentration in the water supplied by the plating company is about 1.21 mg·L$^{-1}$, which is double that in the craft village, where the iron (III) ion concentration is about 0.06 mg·L$^{-1}$. These values exceed the maximum permitted limit concentration of domestic water following the QCVN 02:2009/BYT norm (0.5 mg·L$^{-1}$). The lead (II) ions were not detected in the plating wastewater.

Experiments were performed in the following conditions: 0.03 g of hydroxyapatite was placed in 50 mL of wastewater primarily filtered to remove solid impurities suspended in the solution. After the filtration, the adsorbent was stirred for 45 min, likewise, the experiments described above. Then, the sample was centrifuged to separate the adsorbent from the suspension, and the solution was tested with the application of the AAS technique. Besides, the pH of the plating wastewater is very low, out of the range for domestic water (pH 6.0–8.5). After treatment, the pH of the solution increases, and the concentration of $Fe^{3+}$ is 0.38 mg·L$^{-1}$, smaller than 0.5 mg·L$^{-1}$; the adsorption efficiency is 68.24% in the case of plating wastewater. The $Fe^{3+}$ concentration in craft-village wastewater after adsorption is below the detection limit, indicating an efficiency close to 100%. It can

**Table 6** The values of concentration, pH, H, and Q of the adsorption process in real wastewater

| Wastewater | $C_o$ $Pb^{2+}$ | $C_o$ $Fe^{3+}$ | $pH_{before}$ | $C_e$ $Fe^{3+}$ | $pH_{after}$ | $H_{Fe}$ (%) | $Q_{Fe}$ (mg·g$^{-1}$) |
|---|---|---|---|---|---|---|---|
| Plating | - | 1.21 | 2.70 | 0.38 | 3.74 | 68.24 | 1.37 |
| Craft village | - | 0.06 | 7.54 | 0 | 7.90 | 100 | 0.09 |

be concluded that hydroxyapatite can be used as an effective absorbent for heavy metals removal from wastewater. Its application also can be used on a larger, industrial scale.

### 3.9 Crystallinity, FTIR, and EDX analysis

Remember that the removal of metal ions by HAp adsorbent follows second-order kinetics and the Langmuir adsorption isotherm model. This allows us to predict that metal ion adsorption will occur mostly on the surface and form chemical linkages. For a better understanding, the adsorbent has been analyzed both before and after the adsorption process. Figure 13 shows the XRD patterns and FTIR spectra of the HAp before and after the heavy metal ions removal.

Characteristic peaks of hydroxyapatite were detected, with the highest intensity peak at around 32.5° and another peak at about 26.2° that corresponds to the (211) and (002) planes, respectively, while the other peaks are also in good agreement with the hydroxyapatite structure (Phuong et al., 2020). After Pb ion adsorption, the XRD pattern of the material has changed remarkably. The appearance of the maximum peak at 30.7°, which is indicative of lead hydroxypyromorphite – $Pb_{10}(PO_4)_6(OH)_2$ and various peaks were recorded (Ellis et al., 2006; Hopwood et al., 2016; Zhu et al., 2015), whereas the maximum peak of HAp was found a considerable decrease. This demonstrates that the exchange of ions in aqueous solution between $Ca_{10}(PO_4)_6(OH)_2$ and $Pb^{2+}$ results in a $Ca^{2+}$ substitution in the structure and the formation of $Pb_{10}(PO_4)_6(OH)_2$ (Wang et al., 2019).

Similar to lead ions, $Fe^{3+}$ adsorption also changes the structure of HAp, leading to the formation of the new phase – goethite – FeO(OH), where the peaks at about 12.1°, 17.1°, 27.1°, 35.4°, 39.5°, 52.4°, 56.3°, and 68.2° confirm the goethite presence in the sample (Ghosh et al., 2012; Jiang et al., 2002; Kato et al., 2018; Zilm et al., 2016). However, not all calcium ions are substituted with iron ions. It is worth mentioning that post-treated HAp changes its color, proving effective in ion capturing (Qian et al., 2014). XRD results confirm the effectiveness of the HAp for the removal of heavy ions is due to an ion-exchange mechanism (metal ion ➔ $Ca^{2+}$) that is a main participant in the adsorption process. This result was confirmed by the desorption of $Ca^{2+}$ exchange cation in the solution after adsorption against the amount of $Pb^{2+}$ and $Fe^{3+}$ that were adsorbed (Table 7).

The FTIR spectra of hydroxyapatite before and after $Pb^{2+}$ and $Fe^{3+}$ adsorption are shown in Fig. 13b. We can observe the characteristic peaks of $PO_4^{3-}$ at 1040 $cm^{-1}$, 607 $cm^{-1}$, and 567 $cm^{-1}$ corresponding to the asymmetric stretching vibration of P-O bond

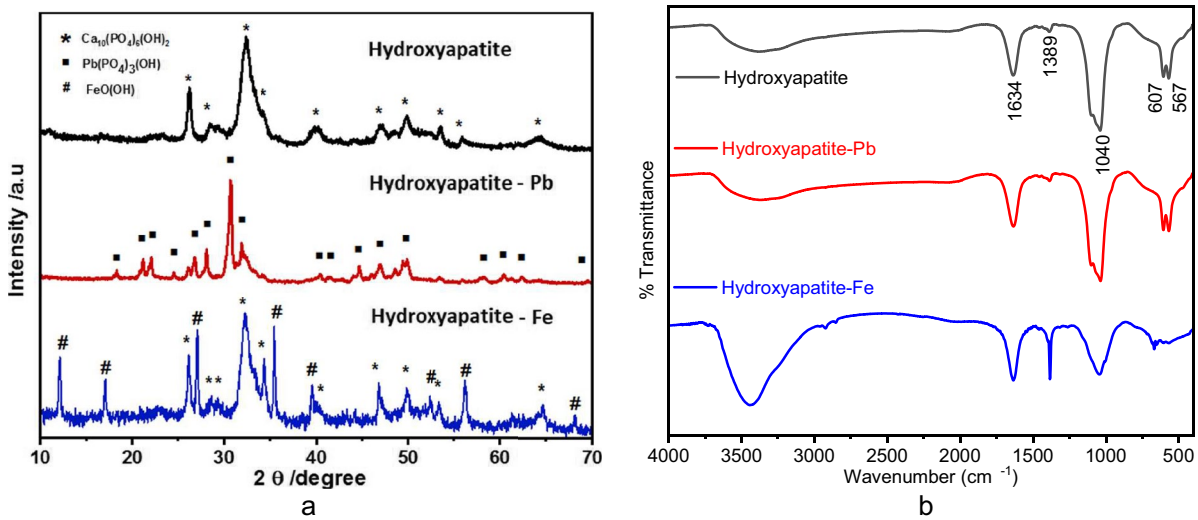


**Fig. 13** XRD patterns (**a**) and IR spectra (**b**) of HAp before and after the adsorption of $Pb^{2+}$ and $Fe^{3+}$

and the asymmetric bending vibration of O-P-O. The bending variation of the $OH^-$ group is characterized by a peak at 1617 $cm^{-1}$. The peak at 1389 $cm^{-1}$ is attributed to $NO_3^-$ group in the modification process (Phuong et al., 2020). After $Pb^{2+}$ and $Fe^{3+}$ adsorption, the spectrum of material still does not change much because of the functional group of $PO_4^{3-}$ and $OH^-$ in $Pb_5(PO_4)_3(OH)$ and HAp.

The change in the distribution and content of Ca, Fe, and Pb present in HAp materials will be confirmed by SEM-EDX analysis results.

Furthermore, the Pb and Fe composition on the surface of the sorbents was also determined by energy-dispersive X-ray spectroscopy (EDX). The elemental composition of the HAp before and after the adsorption was examined at different points on the SEM images (described in Fig. 14). The average atomic and mass compositions are shown in Table 8.

The elemental mapping and spectra for Pb- and Fe-treated samples have been recorded and reveal the uniform distribution of the elements on the material's surface after the removal of metal ions from water. It denotes the existence of metal ions such as $Pb^{2+}$ and $Fe^{3+}$ in the adsorbent after the adsorption. In addition, EDX analyses confirm the dosage of separated atomic and mass composition in the material. The amount of Ca decreases, and the amount of Pb and Fe increases after adsorption. The Ca/P ratio of hydroxyapatite is 1.60, approximately 1.67 of stoichiometry HAp, but after Pb and Fe adsorption, the Ca/P ratio is only 1.40 and 1.22, correspondingly.

## 4 Conclusions

In this work, HAp was successfully synthesized from apatite ore by chemical modification toward efficient and economical water purification. The obtained material exhibited nanostructures with high thermal stability and high porosity. Moreover, the presence of ink-bottle-shaped mesopores and negative surface potential encouraged the use of this material as an adsorbent for heavy metal removal in wastewater. The adsorption results showed that a small amount (around 10 mg) of hydroxyapatite could effectively remove $Pb^{2+}$ from the solution of 50 $mg{\cdot}L^{-1}$ ions concentration having 50 mL in volume at $pH_0$ after

**Table 7** The concentration of $Pb^{2+}$, $Fe^{3+}$, and $Ca^{2+}$ in the solution before and after the adsorption

| Ion | Sample | C $Pb^{2+}$ ($mg{\cdot}L^{-1}$) | H $Pb^{2+}$ (%) | C $Ca^{2+}$ ($mg{\cdot}L^{-1}$) |
|---|---|---|---|---|
| $Pb^{2+}$ | Before adsorption | 82.98 | 97.87 | |
| | After adsorption | 1.76 | | 4.55 |
| Ion | Sample | C $Fe^{3+}$ ($mg{\cdot}L^{-1}$) | H $Fe^{3+}$ (%) | C $Ca^{2+}$ ($mg{\cdot}L^{-1}$) |
| $Fe^{3+}$ | Before adsorption | 24.85 | 91.35 | |
| | After adsorption | 2.15 | | 17.84 |

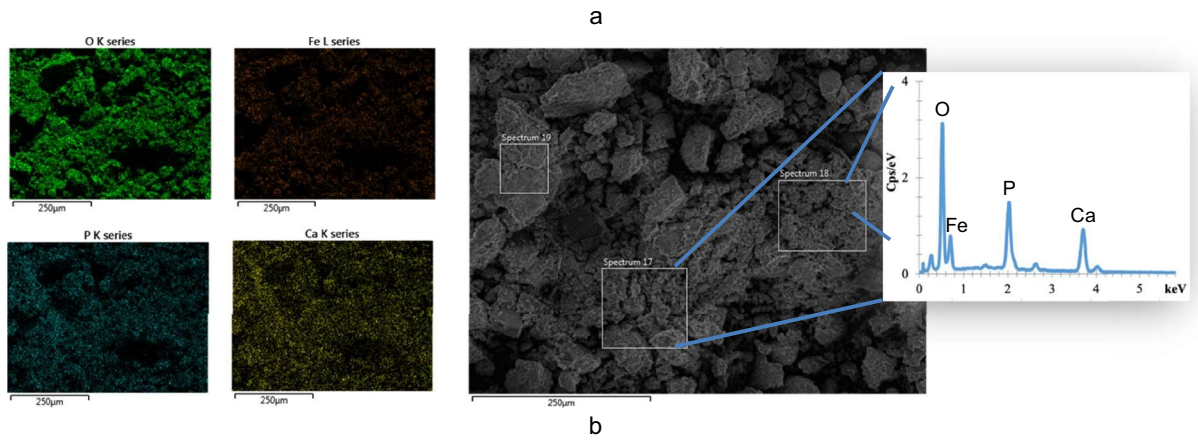


**Fig. 14** SEM-EDX results (particular elements distribution, SEM, and spectrum) obtained for the HAp after the treatment for $Pb^{2+}$ (**a**) and $Fe^{3+}$ (**b**)

**Table 8** Element composition (atomic and mass) of HAp materials before and after the adsorption

| Element | Adsorbent before and after the metal ion adsorption | | | | | |
|---|---|---|---|---|---|---|
| | HAp | | HAp-Fe | | HAp-Pb | |
| | % a | % m | % a | % m | % a | % m |
| O | 54.6 | 37.7 | 52.6 | 34.5 | 53.6 | 27.7 |
| P | 13.3 | 17.8 | 6.2 | 7.9 | 9.7 | 9.9 |
| Ca | 21.3 | 36.7 | 8.7 | 14.4 | 11.8 | 15.2 |
| Fe | | | 13.9 | 32.0 | 0 | 0.0 |
| Pb | | | 0 | 0.0 | 5.8 | 38.4 |
| C | 6.5 | 3.6 | 13.5 | 6.1 | 12.8 | 4.9 |
| Others | 4.3 | 4.2 | 5.1 | 5.1 | 6.3 | 3.9 |
| Total | 100.0 | 100.0 | 100.0 | 100.0 | 100.0 | 100.0 |
| Ca/P | 1.60 | | 1.40 | | 1.22 | |

40 min. Under the same conditions, the $Fe^{3+}$ ions were also removed effectively but after a much longer contact time of 80 min. The kinetics of $Pb^{2+}$ and $Fe^{3+}$ adsorption followed the pseudo-first-order model, where the non-linear equations were used. Based on the obtained results, it can be assumed that the occupation of the adsorption sites is proportional to the number of unoccupied sites on the adsorbent. In order to predict the best isotherm equation that describes the adsorption, non-linear Langmuir, Freundlich, and Redlich-Peterson models were used. The highest values of the correlation coefficient for adsorption of both $Pb^{2+}$ and $Fe^{3+}$ were for a Redlich-Peterson isotherm, assuming the mix of Langmuir and Freundlich models. Interestingly, the literature mainly proposes the Langmuir model, while in some works, the Redlich-Peterson isotherm fitting is not presented in the case of the $Fe^{3+}$ removal with HAp. The maximum adsorption capacity of 342.2 $mg \cdot g^{-1}$ for $Pb^{2+}$ is in good agreement with the literature. Interestingly, the adsorption capacity for $Fe^{3+}$ obtained by HAp proposed here is about 1089.59 $mg \cdot g^{-1}$ which is much higher than described elsewhere for the HAp made from different sources, e.g., bone-derived HAp. Thermodynamic parameters confirm that the adsorption process is spontaneous and feasible. Based on the optimization studies for the model pollutants, the studies were also performed for real wastewater. It is seen that the nanostructural HAp works effectively in water purification. It makes the HAp synthesized from natural apatite ore a cost-effective, affordable, and efficient solution for the removal of these contaminants from aqueous solutions in practical conditions.

**Acknowledgements** M.O. would like to thank Paulina Pietrzyk from the Institute of Fundamental Technological Research Polish Academy of Sciences for valuable consultations.

**Availability of data and materials** The authors can confirm that all relevant data are included in the article.

**Author Contribution** All authors contributed to the study's conception and design. Material preparation, data collection, and analysis were performed by Nguyen Thu Phuong, Nguyen Hong Nam, Dang Vu Qui Dac, and Cao Thi Hong. The first draft of the manuscript was written by Nguyen Thu Phuong and Dinh Thi Mai Thanh, and all authors commented on previous versions of the manuscript. All authors read and approved the final manuscript.

Conceptualization: Nguyen Thu Phuong, Dinh Thi Mai Thanh; methodology: Nguyen Thu Phuong, Nguyen Hong Nam; formal analysis and investigation: Cao Thi Hong, Dang Vu Qui Dac, Nguyen Hong Nam, Do Thi Hai; validation: Nguyen Thu Phuong, Magdalena Osial; writing – original draft preparation: Nguyen Thu Phuong, Dang Vu Qui Dac; writing – review and editing: Nguyen Thu Phuong, Dinh Thi Mai Thanh, Magdalena Osial, Nguyen Hong Nam, Michael Giersig, Le Phuong Thu; funding acquisition: Nguyen Thu Phuong; Resources: Nguyen Thu Phuong; supervision: Dinh Thi Mai Thanh, Nguyen Thu Phuong.

**Funding** This research was funded by the Vietnam Academy of Science and Technology (VAST) under grant no. VAST07.02/20-21.

**Declarations**

**Ethical Approval** Not applicable.

**Consent to Participate** All authors consent to participate in this work.

**Consent for Publication** All authors consent to publish this work.

**Completing Interests** The authors declare no competing interests.

## Appendix

### Calibration curve

To estimate the effectiveness of the nanostructural hydroxyapatite in removing heavy metal ions, the calibration curve was initially measured using 0.1–10 mg·$L^{-1}$ of $Pb^{2+}$ and $Ca^{2+}$ and 0.2–6 mg·$L^{-1}$ of $Fe^{3+}$ solutions with the atomic absorption spectrometry (AAS). Figure 15 shows the calibration curves for $Pb^{2+}$, $Fe^{3+}$, and $Ca^{2+}$ ions used to determine the concentration, adsorption efficiency, and capacity of this study.

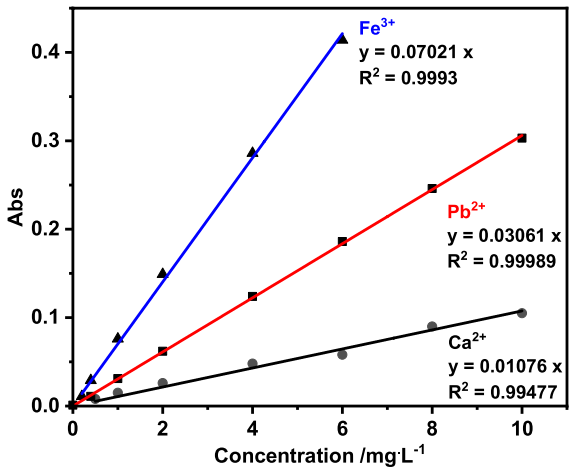


**Fig. 15** The calibration curves for $Pb^{2+}$, $Fe^{3+}$, and $Ca^{2+}$

## References

Abdallah, A., Othmane, A., Younes, E., Houda, M., Nawal, S., & Mohamed, Z. (2021). Copper loaded hydroxyapatite nanoparticles as eco-friendly Fenton-like catalyst to effectively remove organic dyes. *Journal of Environmental Chemical Engineering, 9*, 105501. https://doi.org/10.1016/j.jece.2021.105501

Andrade, V. L., Cota, M., Serrazina, D., Mateus, M. L., Aschner, M., & Santos, A. P. M. (2020). Metal environmental contamination within different human exposure context-specific and non-specific biomarkers. *Toxicology Letters, 324*, 46–53. https://doi.org/10.1016/j.toxlet.2019.12.022

Avakyan, L., Paramonova, E., Bystrov, V., Coutinho, J., Gomes, S., & Renaudin, G. (2021). Iron in hydroxyapatite: interstitial or substitution sites? *Nanomaterials, 11*(11), 2978. https://doi.org/10.3390/nano11112978

Bailliez, S., Nzihou, A., Beche, E., & Flamant, G. (2004). Removal of lead (Pb) by hydroxyapatite sorbent. *Process Safety and Environmental Protection, 82*(B2), 175–180. https://doi.org/10.1205/095758204322972816

Bambaeero, A., & Bazargan – Lari, R. (2021). Simultaneous removal of copper and zinc ions by low cost natural snail shell/hydroxyapatite/chitosan composite. *Chinese Journal of Chemical Engineering, 33*, 221–230. https://doi.org/10.1016/j.cjche.2020.07.066

Billah, R. E. K., Haddaji, Y., Goudali, O., Agunaou, M., & Soufiane, A. (2021). Removal and regeneration of iron (III) from water using new treated fluorapatite extracted from natural phosphate as adsorbent. *Biointerface Research in Applied Chemistry, 11*(5), 131130–113140. https://doi.org/10.33263/BRIAC115.1313013140

Bouiahya, K., Es-saidi, I., Bekkali, C. E., Laghzizil, A., Robert, D., Nunzi, J. M., & Saoiabi, A. (2019). Synthesis and properties of alumina-hydroxyapatite composites from natural phosphate for phenol removal from water. *Colloid and Interface Science Communications, 31*, 100188. https://doi.org/10.1016/j.colcom.2019.100188

Brundavanam, S., Poinern, G. E. J., & Faucett, D. (2015). Kinetic and adsorption behaviour of aqueous Fe2+, Cu2+ and Zn2+ using a 30 nm hydroxyapatite based powder synthesized via a combined ultrasound and microwave based technique. *American Journal of Materials Science, 5*(2), 31–40. https://doi.org/10.5923/j.materials.20150502.02

Cedric, V., Sebastien, R., Ange, Z., Danial, G., Gilles, F., & Patrick, J. S. (2007). Preparation of high specific surface area hydroxyapatite for environmental applications. *Journal of Materials Science, 42*, 6062–6066. https://doi.org/10.1007/s10853-006-1160-y

Chen, M., Wang, X., & Zhang, H. (2021). Comparative research on selective adsorption of Pb(II) by biosorbents prepared by two kinds of modifying waste biomass: Highly-efficient performance, application and mechanism. *Journal of Environmental Management, 288*, 112388. https://doi.org/10.1016/j.jenvman.2021.112388

Cleibson, O., André, L. M. O., Laís, C., Richard, L., Santiago, M.-C., María, D. M. O., Edson, C. S. F., & Maria, G. F. (2021). Zinc (II) modified hydroxyapatites for tetracycline removal: Zn (II) doping or ZnO deposition and their influence in the adsorption. *Polyhedron, 194*, 114897. https://doi.org/10.1016/j.poly.2020.114879

Duyen, L. T., Thao, L. T. P., Hai, D. T., Dung, P. T., Nam, P. T., Thom, N. T., Hong, C. T., Linh, C. T., & Thanh, D. T. M. (2018). Removal of $Cd^{2+}$ by hydroxyapatite adsorption granule from aqueous solution. *Vietnam Journal of Chemistry, 56*(5), 542–547. https://doi.org/10.1002/vjch.201800044

Ellis, D. E., Terra, J., Warschkow, O., Jiang, M., González, G. B., Okasinski, J. S., Bedzyk, M. J., Rossi, A. M., & Jean-Guillaume, E. (2006). A theoretical and experimental study of lead substitution in calcium hydroxyapatite. *Physical Chemistry Chemical Physics, 8*, 967–976. https://doi.org/10.1039/b509254j

Fahami, A., Nasiri-Tabrizi, B., Beall, G. W., & Basirun, W. J. (2017). Structural insights of mechanically induced aluminum-doped hydroxyapatite nanoparticles by Rietveld refinement. *Chinese Journal of Chemical Engineering, 25*(2), 238–247. https://doi.org/10.1016/j.cjche.2016.07.013

Ganguli, P., Sarkhel, R., & Das, P. (2020). Synthesis of pyrolyzed biochar and its application for dye removal: Batch, kinetic and isotherm with linear and non-linear mathematical analysis. *Surfaces and Interfaces, 20*, 100616. https://doi.org/10.1016/j.surfin.2020.100616

Ghosh, M. K., Poinern, G. E. J., Issa, T. B., & Singh, T. B. (2012). Arsenic adsorption on goethite nanoparticles produced through hydrazine sulfate assisted synthesis method. *Korean Journal of Chemical Engineering, 29*, 95–102. https://doi.org/10.1007/s11814-011-0137-y

Harja, M., & Ciobanu, G. (2018). Studies on adsorption of oxytetracycline from aqueous solution onto hydroxyapatite. *Science of the Total Environment, 628-629*, 36–43. https://doi.org/10.1016/j.scitotenv.2018.02.027

Hashimoto, Y., Taki, T., & Sato, T. (2009). Sorption of dissolved lead from shooting range soils using hydroxyapatite amendments synthesized from industrial byproducts as affected by varying pH conditions. *Journal of Environmental Management, 90*, 1782–1789. https://doi.org/10.1016/j.jenvman.2008.11.004

Hopwood, J. D., Derrick, G. R., Brown, D. R., Newman, C. D., Haley, J., Kershaw, R., & Collinge, M. (2016). The identification and synthesis of lead apatite minerals formed in lead water pipes. *Journal of Chemistry, 2016*, 9074062. https://doi.org/10.1155/2016/9074062

Huong NTL, Masami O, Li L, Higashi T, Kanayama M (2010) Heavy metal contamination of river sediments in Vietnam. *Proceedings of the Institution of Civil Engineers – Water Management, 163*(3), 111–121. https://doi.org/10.1680/wama.2010.163.3.111

Huang, R., Lin, Q., Zhong, Q., Zhang, X., Wen, X., & Luo, H. (2020). Removal of Cd(II) and Pb(II) from aqueous solution by modified attapulgite clay. *Arabian Journal of Chemistry, 13*(4), 4994–5008. https://doi.org/10.1016/j.arabjc.2020.01.022

Husband, P. S., & Boxall, J. B. (2011). Asset deterioration and discolouration in water distribution systems. *Water Research, 45*(1), 113–124. https://doi.org/10.1016/j.watres.2010.08.021

Ibrahim, E.-N., & Abdel-Hameed, I. M. (2022). A review of study on heavy metal concentrations in source of water in Vietnam. *Zagazig Journal of Agricultural Research, 49*(2), 209–219. https://doi.org/10.21608/ZJAR.2022.237617

Iconaru, S. L., Motelica-Heino, M., Guegan, R., Beuran, M., Costescu, A., & Predoi, D. (2018). Adsorption of Pb (II) Ions onto hydroxyapatite nanopowders in aqueous solutions. *Materials, 11*, 2204. https://doi.org/10.3390/ma11112204

Jiang, M., Terra, J., Rossi, A. M., Morales, M. A., Saitovitch, E. M. B., & Ellis, D. E. (2002). $Fe^{2+}/Fe^{3+}$substitution in hydroxyapatite: Theory and experiment. *Physical Review B, 66*, 224107. https://doi.org/10.1103/PhysRevB.66.224107

Joseph, I. V., Tosheva, L., & Doyle, A. M. (2020). Simultaneous removal of Cd(II), Co(II), Cu(II), Pb(II), and Zn(II) ions from aqueous solutions via adsorption on FAU-type zeolites prepared from coal fly ash. *Journal of Environmental Chemical Engineering, 8*(4), 103895. https://doi.org/10.1016/j.jece.2020.103895

Kato, S., Ikeda, S., Saito, K., & Ogasawara, M. (2018). Fe incorporation into hydroxyapatite channels by Fe loading and post-annealing. *Journal of Solid State Chemistry, 265*, 411–416. https://doi.org/10.1016/j.jssc.2018.06.032

Kong, Q., Shi, X., Ma, W., Zhang, F., Yu, T., Zhao, F., Zhao, D., & Wei, C. (2021). Strategies to improve the adsorption properties of graphene-based adsorbent towards heavy metal ions and their compound pollutants: A review. *Journal of Hazardous Materials, 415*, 125690. https://doi.org/10.1016/j.jhazmat.2021.125690

Li, S., Li, S., Wen, N., Wei, D., & Zhang, Y. (2021). Highly effective removal of lead and cadmium ions from wastewater by bifunctional magnetic mesoporous silica. *Separation and Purification Technology, 265*, 118341. https://doi.org/10.1016/j.seppur.2021.118341

Lima, É. C., Adebayo, M. A., & Machado, F. M. (2015). Kinetic and equilibrium models of adsorption. In C. Bergmann & F. Machado (Eds.), *Carbon Nanomaterials as Adsorbents for Environmental and Biological Applications. Carbon Nanostructures*. Springer. https://doi.org/10.1007/978-3-319-18875-1_3

Lima, É. C., Hosseini-Bandegharaei, A., Moreno-Piraján, J. C., & Anastopoulos, I. (2018). A critical review of the estimation of the thermodynamic parameters on adsorption equilibria. Wrong use of equilibrium constant in the Van't Hoof equation for calculation of thermodynamic parameters of adsorption. *Journal of Molecular Liquids, 273*, 425–434. https://doi.org/10.1016/j.molliq.2018.10.048

Lusvardi, G., Malavasi, G., Menabue, L., & Saladini, M. (2002). Removal of cadmium ion by means of synthetic hydroxyapatite. *Waste Manage, 22*(8), 853–857. https://doi.org/10.1016/S0956-053X(02)00078-8

Marjan, S., Ramesh, S., Tan, C. Y., Hari, C., Ching, Y. C., Ahmad, F. M. N., Krishnasamy, S., & Teng, W. D. (2020). Sintering behaviour of carbonated hydroxyapatite prepared at different carbonate and phosphate ratios. *Boletín de la Sociedad Española de Cerámica y Vidrio, 59*(2), 73–80. https://doi.org/10.1016/j.bsecv.2019.08.001

Mavropoulos, E., Rossi, A. M., Costa, A. M., Perez, C. A., Moreira, J. C., & Saldanha, M. (2002). Studies on the mechanisms of lead immobilization by hydroxyapatite. *Environmental Science & Technology, 36*(7), 1625–1629. https://doi.org/10.1021/es0155938

Meski, S., Ziani, S., & Khireddine, H. (2010). Removal of lead ions by hydroxyapatite prepared from the egg shell. *Journal of Chemical & Engineering Data, 55*(9), 3923–3928. https://doi.org/10.1021/je901070e

Minh, D. P., Tran, N. D., Nzihou, A., & Sharrock, P. (2013). Hydroxyapatite gel for the improved removal of $Pb^{2+}$ ions from aqueous solution. *Chemical Engineering Journal, 232*, 128–138. https://doi.org/10.1016/j.cej.2013.07.086

Nam, P. T., Thanh, D. T. M., Phuong, N. T., Trang, N. T. T., Hong, C. T., Anh, V. T. K., Lam, T. D., & Thom, N. T. (2021). Adsorption of $Ag^{+}$ ions using hydroxyapatite powder and recovery silver by electrodeposition. *Vietnam Journal of Chemistry, 59*(2), 179–186. https://doi.org/10.1002/vjch.202000148

Nga, T. M., Minh, N. N., Toshiki, T., Phuong, L. T. N., & Nam, H. N. (2021). Evolution of physico-chemical properties of *Dicranopteris linearis*-derived activated carbon under

various physical activation atmospheres. *Scientific Reports, 11*, 14430. https://doi.org/10.1038/s41598-021-93934-x

Olabiyi, O. G., & Adekola, F. A. (2018). Removal of iron and manganese from aqueous solution using hydroxyapatite prepared from cow bone. *Research & Reviews: Journal of Materials Science, 6*(2), 59–74. https://doi.org/10.4172/2321-6212.1000218

Phuong, N. T., Xuyen, N. T., Trang, N. V., Thom, N. T., Thai, V. Q., Huy, N. T., Nam, P. T., & Thanh, D. T. M. (2020). Treatment of $Cd^{2+}$ and $Cu^{2+}$ ions using modified apatite ore. *Journal of Chemistry, 6527197*. https://doi.org/10.1155/2020/6527197

Pramod, N. J., Pramod, P. J., Meghnad, G. J., & Sambhaji, R. B. (2016). A prototype synthesis and characterization of hydroxyapatite bioceramics nanocrystallites. *Advanced Materials Letters, 7*(4), 325–329. https://doi.org/10.5185/amlett.2016.5837

Qian, G., Li, M., Wang, F., & Liu, X. (2014). Removal of $Fe^{3+}$ from aqueous solution by natural apatite. *Journal of Surface Engineered Materials and Advanced Technology, 4*, 14–20. https://doi.org/10.4236/jsemat.2014.41003

Ragab, A., Ahmed, I., & Bader, D. (**2019**). The removal of brilliant green dye from aqueous solution using nano hydroxyapatite/chitosan composite as a sorbent. *Molecules, 24*, 847. https://doi.org/10.3390/molecules24050847

Ramachandra, R. R., Roopa, H. N., & Kannan, T. S. (1997). Solid state synthesis and thermal stability of HAp and HAp-β-TCP composite ceramic powders. *Journal of Materials Science: Materials in Medicine, 8*, 511–518. https://doi.org/10.1023/A:1018586412270

Ramesh, S. T., Rameshbabu, N., Gandhimathi, R., Srikanth, K. M., & Nidheesh, P. V. (2013). Adsorptive removal of Pb(II) from aqueous solution using nano-sized hydroxyapatite. *Applied Water Science, 3*, 105–113. https://doi.org/10.1007/s13201-012-0064-z

Satoshi, O., Tadafumi, A., Takashi, I., Masatomo, Y., Takeshi, M., Hiroya, A., Yuichi, S., Kiyoshi, N., Minoru, M., Kenji, K., & Akira, O. (2008). Chapter 5 – Characterization methods for nanostructure of material. *Nanoparticle Technology Handbook, 2008*, 267–315. https://doi.org/10.1016/B978-044453122-3.50008-8

Slavica, L., Slavica, Z., Nada, M., & Slobodan, M. (2001). The effect of temperature on the properties of hydroxyapatite precipitated from calcium hydroxide and phosphoric acid. *Thermochimica Acta, 374*(1), 13–22. https://doi.org/10.1016/S0040-6031(01)00453-1

Sridevi, B., Gérrard, E. J. P., & Derek, F. (2015). Kinetic and adsorption behaviour of aqueous Fe2+, Cu2+ and Zn2+ using a 30 nm hydroxyapatite based powder synthesized via a combined ultrasound and microwave based technique. *Am J Mater Sci, 5*(2), 31–40. https://doi.org/10.5923/j.materials.20150502.02

Sugashini, S., & Begum, K. M. M. S. (2013). Column adsorption studies for the removal of Cr(VI) ions by ethylamine modified chitosan carbonized rice husk composite beads with modelling and optimization. *Journal of Chemistry, 2013*, 460971. https://doi.org/10.1155/2013/460971

Tahoon, M. A., Siddeeg, S. M., Alsaiari, N. S., Mnif, W., & Rebah, F. B. (2020). Effective heavy metals removal from water using nanomaterials: a review. *Processes, 8*(6), 645. https://doi.org/10.3390/pr8060645

Thuy, L.T.T, Son, T.H, Khu L.V (2021). Activated carbons from coffee husk: Preparation, characterization, and reactive red 195 adsorption. J Chem Res, 45

Tran, H. N., Lima, É. C., Juan, R. S., Bollinger, J. D., & Chao, H. P. (2021). Thermodynamic parameters of liquid–phase adsorption process calculated from different equilibrium constants related to adsorption isotherms: A comparison study. *Journal of Environmental Chemical Engineering, 9*(6), 106674. https://doi.org/10.1016/j.jece.2021.106674

Tran, H. N., You, S. J., Hosseini-Bandegharaei, A., & Chao, H. P. (2017). Mistakes and inconsistencies regarding adsorption of contaminants from aqueous solutions: A critical review. *Water Research, 120*, 88–116. https://doi.org/10.1016/j.watres.2017.04.014

Vahdat, A., Ghsemi, B., & Yousefpour, M. (2019). Synthesis of hydroxyapatite and hydroxyapatite/$Fe_3O_4$ nanocomposite for removal of heavy metals. *Environmental Nanotechnology, Monitoring & Management, 12*, 100233. https://doi.org/10.1016/j.enmm.2019.100233

Vesali-Naseh, M., Naseh, M. R. V., & Ameri, P. (2021). Adsorption of Pb(II) ions from aqueous solutions using carbon nanotubes: A systematic review. *Journal of Cleaner Production, 291*, 125917. https://doi.org/10.1016/j.jclepro.2021.125917

Wang, M., Wang, X., Zhang, K., Wu, M., Wu, Q., Liu, J., Yang, J., & Zhang, J. (2019). Direct bromination of nano hydroxyapatite strategy towards particle brushes **via** surface-initiated ATRP for highly efficient heavy metal removal. *Polymer, 183*, 121883. https://doi.org/10.1016/j.polymer.2019.121883

Yadav, V. B., Gadi, R., & Kalra, S. (2019). Clay based nanocomposites for removal of heavy metals from water: A review. *Journal of Environmental Management, 232*, 803–817. https://doi.org/10.1016/j.jenvman.2018.11.120

Zhang, Z., Wang, X., Wang, H., & Zhao, J. (2018). Removal of Pb(II) from aqueous solution using hydroxyapatite/calcium silicate hydrate (HAP/C-S-H) composite adsorbent prepared by a phosphate recovery process. *Chemical Engineering Journal, 344*, 53–61. https://doi.org/10.1016/j.cej.2018.03.066

Zhou, Q., Yang, N., Li, Y., Ren, B., Ding, X., Bian, H., & Yao, X. (2020). Total concentrations and sources of heavy metal pollution in global river and lake water bodies from 1972 to 2017. *Global Ecology and Conservation, 22*, e00925. https://doi.org/10.1016/j.gecco.2020.e00925

Zhu, Y., Zhu, Z., Zhao, X., Liang, Y., & Huang, Y. (2015). Characterization, dissolution, and solubility of lead hydroxypyromorphite [$Pb_5(PO_4)_3OH$] at 25-45°C. *Journal of Chemistry, 2015*, 269387. https://doi.org/10.1155/2015/269387

Zilm, M. E., Chen, L., Sharma, V., McDannald, A., Jain, M., Ramprasad, R., & Wei, M. (2016). Hydroxyapatite substituted by transition metals: Experiment and theory. *Physical Chemistry Chemical Physics, 18*, 16457–16465. https://doi.org/10.1039/C6CP00474A